PLANT SCIENCE

Cauliflower fractal forms arise from perturbations of floral gene networks

Eugenio Azpeitia[1]†, Gabrielle Tichtinsky[2], Marie Le Masson[2], Antonio Serrano-Mislata[3], Jérémy Lucas[2], Veronica Gregis[4], Carlos Gimenez[3], Nathanaël Prunet[5,6], Etienne Farcot[7], Martin M. Kater[4], Desmond Bradley[8], Francisco Madueño[3], Christophe Godin[1]*, Francois Parcy[2]*

Throughout development, plant meristems regularly produce organs in defined spiral, opposite, or whorl patterns. Cauliflowers present an unusual organ arrangement with a multitude of spirals nested over a wide range of scales. How such a fractal, self-similar organization emerges from developmental mechanisms has remained elusive. Combining experimental analyses in an *Arabidopsis thaliana* cauliflower-like mutant with modeling, we found that curd self-similarity arises because the meristems fail to form flowers but keep the "memory" of their transient passage in a floral state. Additional mutations affecting meristem growth can induce the production of conical structures reminiscent of the conspicuous fractal Romanesco shape. This study reveals how fractal-like forms may emerge from the combination of key, defined perturbations of floral developmental programs and growth dynamics.

Above-ground plant architectures arise from the activity of shoot apical meristems (SAMs), pools of stem cells that give rise to organs such as leaves, shoots, or flowers. The arrangement of organs on stems is called phyllotaxis. Plants with a spiral phyllotaxis usually form two families of organ spirals that are visible on compact structures such as flower heads, pine cones, or cacti (Fig. 1, A to C). These two families of spirals turn in opposite directions and come in two consecutive numbers of the Fibonacci series (Fig. 1A) (*1*). In cauliflowers, spiral families are visible not only at one but at several scales (Fig. 1, D to F). This self-similar organization culminates in the Romanesco cultivar in which the spirals appear in relief because of their conical shape at all scales, a geometrical feature conferring the whole curd a marked fractal-like aspect (Fig. 1G).

Cauliflowers (*Brassica oleracea* var. *botrytis)* were domesticated from cabbages (*2*). The cauliflower inflorescence (the flower-bearing shoot) takes a curd shape because each emerging flower primordia never matures to the floral stage but instead generates more curd-shaped inflorescences (*2*, *3*). In *B. oleracea,* the genetic modifications causing curd development are still debated and likely affect multiple genes (*2*–*5*). However, cauliflower-like structures also exist in the model Brassicaceae *Arabidopsis thaliana* and are caused by a double mutation in *APETALA1* (*API*) and *CAULIFLOWER* (*CAL*) (Fig. 1, H and I), two paralogous genes encoding MADS-box transcription factors (TFs) promoting floral development (*6*, *7*). The *Arabidopsis* molecular regulators governing the development of shoots and flowers have been largely identified (*8*–*10*) (table S1). Network models based on these regulators have been proposed to explain flower and inflorescence development (*11*–*14*). However, whether variants of these networks are able to account for the development of *Arabidopsis ap1 cal* curds is unknown.

To address this question, we first built a network of the main regulators involved in both flower and curd development. Then, we embedded this network within a three-dimensional (3D) computational model of plant development to understand how mutations could transform wild-type (WT) inflorescences into curds.

Genetic basis of cauliflower curds

In *Arabidopsis*, flowers are initiated by the TF LEAFY (LFY) (Fig. 1J) (table S1). *LFY* is up-regulated by the SUPPRESSOR-OF-OVEREXPRESSION-OF-CO 1 (SOC1) and AGAMOUS-LIKE 24 (AGL24) MADS-box proteins (induced throughout the inflorescence meristem by environmental and endogenous cues) and by auxin phytohormone maxima that mark floral meristem initiation sites. *LFY* is expressed specifically in floral primordia because its induction in the SAM is repressed by the TFL1 inflorescence identity protein. In the floral primordium, LFY induces *API* and *CAL* (*API/CAL*), which positively feedback on *LFY* and repress both *SOC1*/*AGL24* and *TFL1*, thereby stabilizing the floral fate of the new meristem. In the *ap1 cal* cauliflower mutant, the AP1/LFY positive feedback is absent and *TFL1* is not repressed by AP1/CAL in the nascent floral meristem. Consequently, young flower primordia cannot maintain *LFY* expression and start expressing *TFL1*. As a result, they lose their floral identity and become inflorescence meristems (*6*). Whereas *TFL1* repression in nascent flower primordia is well understood, the factors directly responsible for its up-regulation in *ap1 cal* and inflorescence meristems are unknown.

To complete our network, we thus searched for direct positive regulators of *TFL1* other than LFY [which induces *TFL1* (*15*) but is not active in inflorescence meristems]. *TFL1* is indirectly regulated by day length (*16*): During long days (LDs), *TFL1* is up-regulated by CONSTANS (CO) and FLOWERING LOCUS T (FT), two key upstream effectors of the LD pathway (*11*, *17*–*19*) (fig. S1). To search for direct regulators, we examined SOC1 and AGL24, which act downstream of CO and FT in the LD pathway (*9*). Loss- and gain-of-function experiments demonstrated that both SOC1 and AGL24 induce *TFL1* (Fig. 2, A to I) and chromatin immunoprecipitation (ChIP) showed that these two TFs bind to the *TFL1* regions that regulate its expression in the SAM (*20*) (Fig. 2, J to L). These regions were sufficient to activate a *TFL1* reporter construct by SOC1 and AGL24 in a transient assay (Fig. 2, M and N), confirming that both MADS-box TFs are direct regulators of *TFL1*. Because XAANTAL2 (XAL2), a homolog of SOC1 and AGL24, also bound to and induced *TFL1* (*21*), we aggregated the activities of SOC1, AGL24, and XAL2 into a SAX proxy acting as a *TFL1* positive regulator (Fig. 3A).

We thus created the SALT network (for SAX, AP1/CAL, LFY, and TFL1; Fig. 3A) made of these four regulator sets, auxin (*22*), and F, a flower-inducing signal (a proxy for the FT florigen) that increases when the plant ages or is exposed to flower-inducing environmental conditions (*23*, *24*). We also added a short-lived transient early Repressor of *TFL1* (eREP) as a proxy for *TFL1* early repression in the young flower bud performed by the redundant activities of SOC1, AGL24, SHORT VEGETATIVE PHASE, and SEPALLATA4 (*25*).

The steady states of the SALT network correspond to the gene expression patterns observed in WT vegetative (low SALT values), inflorescence (high TFL1/SAX, low AP1/CAL/LFY), and flower (low TFL1/SAX, high AP1/CAL/LFY) meristems (Fig. 3, B and C, and fig. S2). Above a certain F threshold value, the network generates a flower or an inflorescence state depending on F and auxin values. Simulations of *tfl1*, *lfy*, *ap1 cal* mutants produced the expected outputs consistent with experimentally reported gene expressions (*6*, *16*, *26*, *27*) (Fig. 3, B and C). The simulated *sax* mutant did not reach a floral

[1]Laboratoire de Reproduction et Développement des Plantes, Univ. Lyon, ENS de Lyon, UCB Lyon 1, CNRS, INRAE, Inria, F-69364 Lyon, France. [2]Laboratoire Physiologie Cellulaire et Végétale, Univ. Grenoble Alpes, CNRS, CEA, INRAE, IRIG-DBSCI-LPCV, F-38054 Grenoble, France. [3]Instituto de Biología Molecular y Celular de Plantas (IBMCP), Consejo Superior de Investigaciones Científicas (CSIC) - Universidad Politécnica de Valencia (UPV), 46022 Valencia, Spain. [4]Dipartimento di Bioscienze, Università degli Studi di Milano, 20133 Milan, Italy. [5]Division of Biology and Biological Engineering, California Institute of Technology, Pasadena, CA 91125, USA. [6]Department of Molecular, Cell and Developmental Biology, University of California, Los Angeles, CA 90095, USA. [7]School of Mathematical Sciences, University of Nottingham, Nottingham NG7 2RD, UK. [8]Department of Cell and Developmental Biology, John Innes Centre, Norwich NR4 7UH, UK.
***Corresponding author. Email: christophe.godin@inria.fr (C.G.); francois.parcy@cea.fr (F.P.)** †Present address: Centro de Ciencias Matemáticas, Universidad Nacional Autónoma de México, Morelia, México.

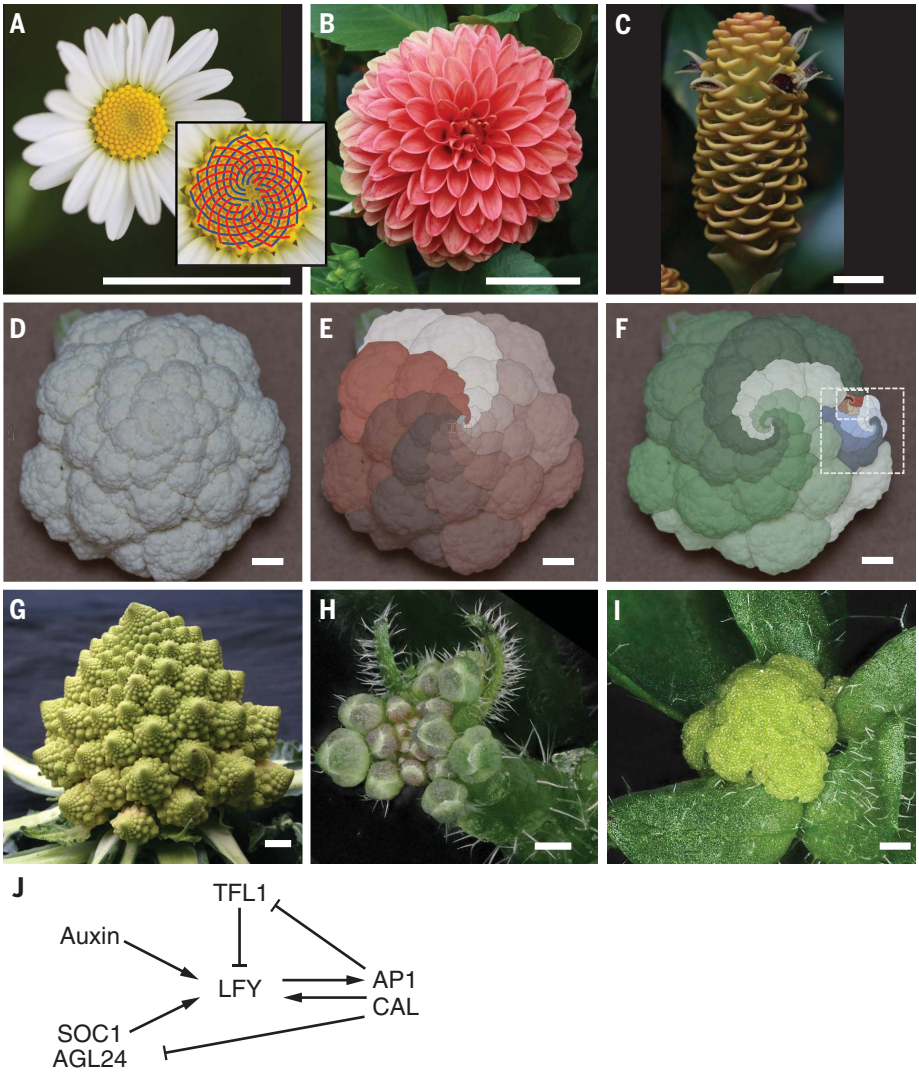

Fig. 1. Illustrations of phyllotactic spirals on plant inflorescences. (**A**) Daisy capitulum. The two families of spirals are indicated in the close-up (13 blue spirals and 21 red). (**B**) Dahlia composite flower. (**C**) Zingiber inflorescence. (**D** to **F**) *B. oleracea* var. *botrytis* cauliflower with eight counterclockwise [(E); brown family] and five clockwise [(F); green family] main spirals. Dashed rectangles show families of spirals nested over several scales. (**G** to **I**) Romanesco curd (G), *Arabidopsis* WT inflorescence (H), and *ap1 cal* curd (I). Scale bars, 2 cm [(A) to (G)]; 500 μm [(H) and (I)]. (**J**) Interactions between major floral regulators; arrows depict activation and barred lines indicate repression.

state, consistent with the late-flowering behavior of the *soc1 agl24* double mutant (*28*).

The modeled gene expression dynamics (Fig. 3D) illuminate the fundamental differences between WT and cauliflower meristems: In a WT flower primordium, F induces *SAX*. SAX and auxin induce *LFY*, which, together with F, induces *AP1/CAL*. AP1 positively feeds back on *LFY* and represses *SAX* (Fig. 3D). *TFL1* expression, which could be induced by SAX and LFY in early floral stages, is constantly repressed, first by eREP and later by SAX plus AP1/CAL. High AP1/CAL and LFY with low TFL1 and SAX expression stabilize the floral fate. By contrast, in the *ap1 cal* flower primordia, the absence of AP1/CAL activity has two consequences: (i) *LFY* expression is up-regulated only transiently because AP1/CAL positive feedback is missing (Fig. 3D) and (ii) *SAX* genes are not repressed by AP1 and thus induce *TFL1* in nascent flower meristems. TFL1 represses *LFY* even further and the meristem returns to a shoot meristem state (Fig. 3D). The early LFY induction would likely be reinforced (while remaining transient) by incorporating the recently discovered direct induction of LFY by the F partner protein FD (*29*). The SALT model predicts that *SAX* expression should extend over the entire cauliflower. We analyzed a SOC1-GFP reporter line and indeed observed expansion of its expression domain in *ap1 cal* compared with WT (Fig. 3, E and F).

The SALT network thus recapitulates realistic gene expressions driving meristem fates. However, a plant architecture depends not just on meristem fates but also on morphodynamic parameters, including molecular thresholds for fate decisions, organ growth rate, delay for meristems to start organ production, and organ production rate, which are independently regulated. Plant inflorescence architecture thus emerges from the complex interaction between the floral gene-regulatory network (GRN) and morphodynamic parameters. This is illustrated here by the *lfy* and *ap1 cal* mutants that have the same GRN outputs (Fig. 3C) but markedly different architectures (*6*, *27*). To study how this interaction operates in *Arabidopsis*, we integrated the SALT GRN in a 3D plant computational model implemented as an L-system (see the supplementary materials, modeling methods).

A multiscale model generates *Arabidopsis* cauliflower structures

The 3D model is made of the four types of organs that shape plant above-ground architecture: meristems, internodes, leaves, and flowers (Fig. 4A and see the supplementary materials). Each meristem's identity (vegetative, inflorescence, and floral) is determined by the GRN steady state, computed at each time step as a function of the meristem's previous state and external factors (auxin and F). The GRN model is implemented as single-compartment ordinary differential equations (see the supplementary materials, modeling methods). We assume that the GRN dynamics are faster than growth and reach steady state within a time step. A set of growth rules defines meristem production: A vegetative meristem produces a compressed stem (non-elongated internodes) with rosette leaves and dormant axillary meristems; an inflorescence meristem produces an elongating internode with either a cauline leaf and a new axillary shoot meristem in the leaf axil or a lateral flower meristem; and a floral meristem produces an internode terminating with a flower meristem devoid of bracts (leaf-like organs subtending flowers) because they are repressed by LFY (*6*). Each newly generated axillary meristem begins with maximal auxin level (*22*), SAX/LFY/AP1/CAL values inherited from the parent meristem, together with a fraction of the parent TFL1 value because in the real plant, this non–cell-autonomous protein is present in the primordia region (*30*). To match the WT plant architecture, indeterminate meristems at orders >2 (Fig. 4A) were kept quiescent, a likely effect of apical dominance (the inhibition of lateral meristem outgrowth) (fig. S3A). The model also contains rules describing organ growth dynamics (internode and leaf elongation, flower growth, organ production rate, and growth initiation delay). Simulated plants start with a single vegetative SAM and repeatedly

Erratum 10 December 2021. See Erratum.

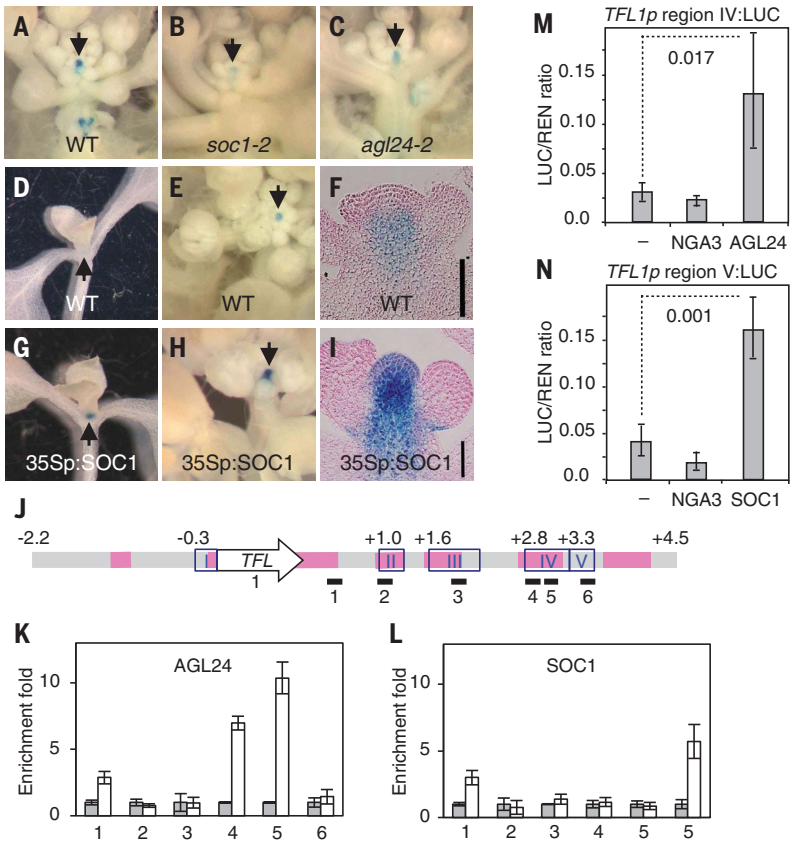

Fig. 2. AGL24 and SOC1 are direct positive regulators of *TFL1*. (**A** to **C**) TFL1p:GUS activity in WT (A), *soc1-2* (B), and *agl24-2* (C) inflorescence apices. (**D** to **I**) TFL1p:GUS activity (blue signal) in WT [(D) to (F)] and *35Sp:SOC1* [(G) to (I)] apices at the vegetative [(D) and (G)] and flowering [(E), (F), (H), and (I)] stages. (F) to (I) are longitudinal sections through flowering shoots. Arrows mark the SAM. Scale bars in (F) and (I), 40 μm. (**J** to **L**) Structure of *TFL1* locus, with regions conserved in Brassicaceae (pink lines), regulatory regions (*20*) (blue boxes I to V), and fragments used in ChIP (black lines 1 to 6). ChIP experiments on plants expressing a tagged version of AGL24 [(K), white bars] or the WT SOC1 protein [(L), white bars] or on control plants [(K) and (L), gray bars; see the supplementary materials and methods] showed that AGL24 binds region IV [(K), fragments 4 and 5] and SOC1 region V [(L), fragment 6]. A representative biological replicate is shown with the mean ± SE for three technical replicates. (**M** and **N**) Transient assays showing transactivation of the LUCIFERASE (LUC) reporter driven by region IV (activation by 35Sp:AGL24) and region V (activation by 35Sp:SOC1). NGA3 is an unrelated TF used as a negative control. Bars denote the mean ± SD of three independent biological replicates. *P* values are for the equality of means (Student's *t* test).

produce new organs according to the GRN, the morphodynamic rules, and an input value of F.

By adjusting the GRN and morphodynamic parameters within a range of plausible values (see the supplementary materials), we successfully calibrated the model to produce realistic architectures for WT and *lfy* plants (movies S1 and S2), as well as for the *tfl1* mutant (Fig. 4, B to D) and a nonflowering phenotype for the *sax* mutant. However, our simulations could not generate a realistic *ap1 cal* mutant growing without bract or cauline leaves and displaying high-order meristems (fig. S3, A and B), suggesting that the cauliflower phenotype involves additional regulations. We reasoned that laterally produced *ap1 cal* inflorescence meristems are different from those produced in other genotypes because according to our GRN, they have been transiently exposed to LFY expression (Fig. 3D). Several pieces of evidence suggest that this transient LFY expression, already known to repress bracts (*6*), could also contribute to high-order meristem release. First, the outgrowth of otherwise inhibited axillary meristems in the rosette is stimulated by ectopic expression of LFY (or an LFY allele) (*31*, *32*). Second, it was established that the *lfy ap1 cal* triple mutant does not form cauliflowers (*6*), and we found that in this mutant, the number of high-order meristems was significantly reduced compared with *ap1 cal* (fig. S3, D to H), thus supporting our hypothesis.

We abstracted this critical molecular pathway by introducing in the model a factor X up-regulated when LFY exceeds a minimal threshold level. Up-regulated factor X releases high-order meristem growth and suppresses the bract. This was sufficient to unlock the recursive growth of lateral meristems and to generate the *ap1 cal* curd structure that arises from the transient but irreversible exposure of meristems to the floral signal without any alteration of WT growth dynamics (Fig. 4, E and H, and movie S3). Overall, our work shows that the *ap1 cal* and *lfy* architectures are different (Fig. 3C) because the molecular histories of their inflorescence meristems are different, thereby revealing the existence of a developmental hysteresis.

Growth dynamics define cauliflower and Romanesco curd structures

Our work in *Arabidopsis* offers a conceptual framework to explain how inflorescence architecture emerges from coupling a floral GRN to morphodynamic parameters. We wondered whether modifications affecting components of this framework could also explain the architecture of the cauliflowers that arose during domestication, namely the edible *B. oleracea (Bo)* var. *botrytis (Bob)* and its Romanesco variant. Whether similar genetic defects as in *Arabidopsis* are responsible for curd development in *B. oleracea* is still debated (*4*, *5*). To further investigate this point, we analyzed RNA-sequencing data of *Bob* curds. We confirmed the previously identified mutation in the *BobCAL* gene (fig. S4A) (*4*, *5*, *7*) and observed that the two *AP1* paralogs, *BobAP1-a* and *BobAP1-c*, are expressed at much lower levels than in cabbage (*Bo* var. *capitata)* inflorescences (fig. S4B). These functional proteins are induced with a delay only when the cauliflower elongates and starts forming normal flowers (*3*, *33*). Comparing cauliflower and cabbage sequences, we identified differences in binding sites for candidate regulators of *BoAP1* that could account for their delayed activation (fig. S4D). The combination of BoCAL inactivation and *BobAP1-a/c* expression delay (heterochrony caused by *cis* or *trans* mutations) thus likely participates in *Bob* curd development. Similar to *Arabidopsis ap1 cal*, cauliflowers have meristems of higher maximal order ($n \geq 7$) than cabbages ($n = 3$ to 4) (fig. S5). Nevertheless, the development of single massive cauliflower curds is not the exact equivalent of the *Arabidopsis* mutant (*3*, *5*) and involves additional multifactorial alterations of morphodynamics parameters (such as reduction of internode elongation and increase in branch diameter).

The conical shapes appearing in Romanesco spirals at all scales (Fig. 1F) represent an additional geometric variation obtained through domestication that seems to be associated with a change in morphodynamic parameters. Indeed, several such parameters remain constant during cauliflower development but vary in Romanesco (*34*): (i) the plastochron, the time between two successive meristem productions, (ii) the number of visual spirals originating from a given meristem, (iii) the time

Erratum 10 December 2021. See Erratum.

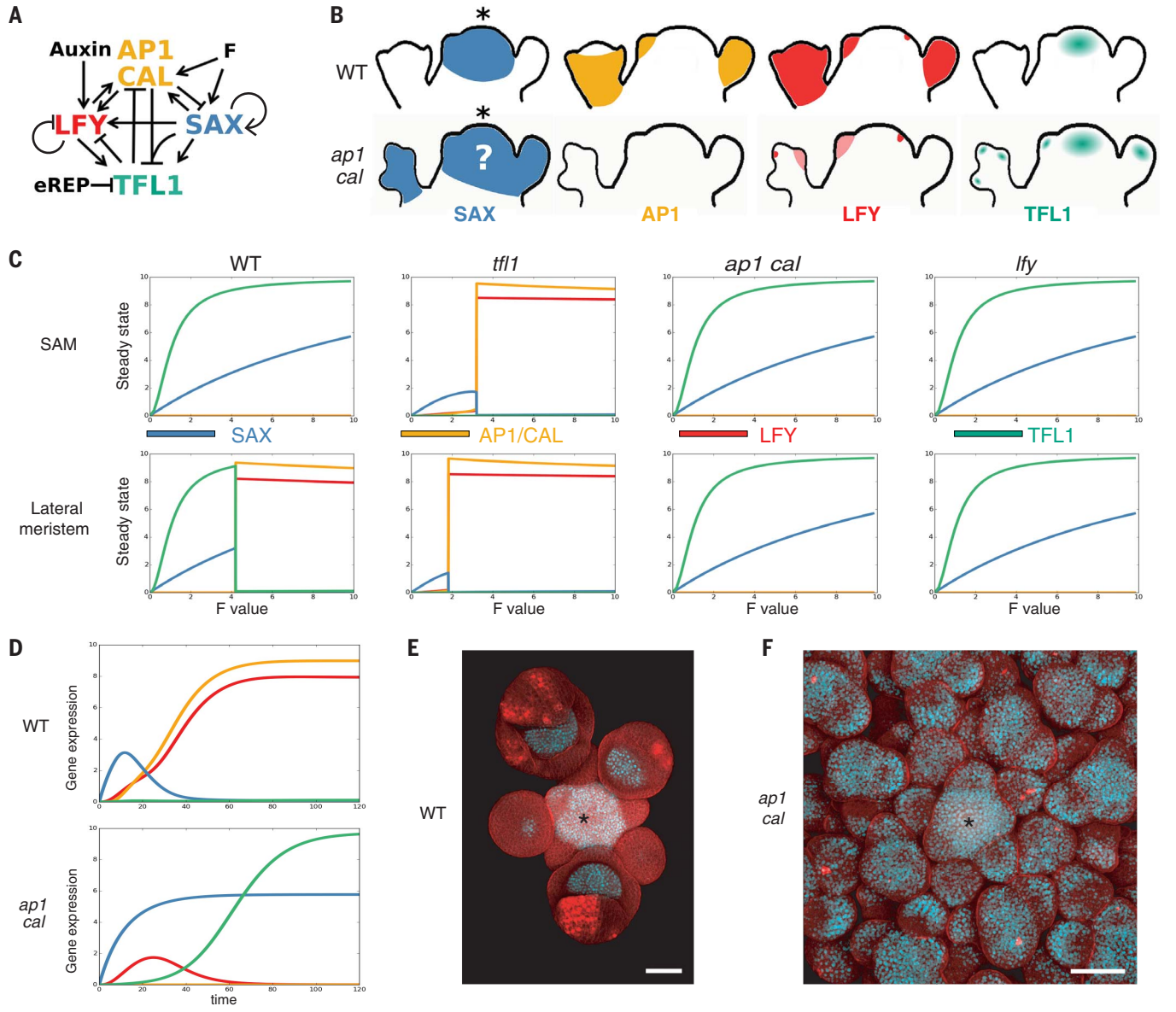

Fig. 3. SALT GRN model and experimental validation. (**A**) SALT GRN network structure. (**B**) Known expression patterns of *SAX*, *AP1/CAL*, *LFY*, and *TFL1* in the SAM and lateral primordia of the WT and the *ap1 cal* mutant. The question mark indicates a predicted expression pattern of the model. (**C**) WT, *tfl1*, *ap1 cal*, and *lfy* steady states of the model at different F values in the SAM (low auxin) and in lateral meristems (high auxin). The genetic identity predicted for WT and all mutant meristems correspond to the experimentally observed phenotypes. (**D**) Temporal simulation of gene expression in lateral primordia with high F values. (**E** and **F**) Expression of the SOC1:GFP (white/light blue signal) reporter construct in WT (E) and *ap1-7 cal-1* mutant (F) inflorescences. Asterisks mark the SAM. Scale bars, 50 μm.

(measured in number of plastochrons) needed before a lateral primordium starts producing its own primordia (or lateral production onset delay), and (iv) the size of the meristems. Whether some of these parameters are causal to the Romanesco phenotype remains unclear, but phyllotaxis studies (*1*, *35*, *36*) indicate that the first three parameters are linked to the meristem size: An augmentation of the size of the meristem central zone should decrease the plastochron, which in turn increases the number of spirals, and the lateral production onset delay. We thus hypothesized that passing from a constant to a decreasing plastochron in meristems could change cauliflower into Romanesco morphologies by increasing the internode insertion pace on each axis. As the internode elongation rate remains unchanged, this accelerates the axis elongation compared to its laterals. We first tested this in silico using a simplified, purely geometric model of curd growth that is independent from the *Arabidopsis* GRN and specific growth dynamics (see the supplementary materials). A decreasing plastochron was sufficient to produce Romanesco shapes, whereas constant values of this parameter produce cauliflower morphologies (Fig. 4, F and G, fig. S6, and movies S4 and S5).

We then introduced the same change in the more complex, GRN-based *Arabidopsis* cauliflower architectural model while keeping its organ growth dynamics as calibrated on the WT. Although not as complete as in the purely geometric model, the curd changed toward a "Romanesco-like" morphology with typical conical curd shapes (Fig. 4, H and I). We then tested this hypothesis experimentally in *Arabidopsis* by altering the size of the meristem directly. We achieved this by introducing

Erratum 10 December 2021. See Erratum.

a mutation in the *CLAVATA3* (*CLV3*) gene that controls meristem homeostasis and induces an increase of the meristem central zone during growth (*37*, *38*). As predicted by our analysis, introduction of a *clv3* mutation in *ap1 cal* *Arabidopsis* mutant modified the curd shape, which lost its round morphology and acquired a more conical shape, with similar structures at different scales, features recognized as hallmarks of Romanesco curds (*39*) (Fig. 4, L and M). Two additional pieces of evidence support the hypothesis that meristem homeostasis is perturbed in Romanesco curds: (i) they occasionally show fasciation, a feature typical of meristem enlargement also observed in *clv3* or *ap1 cal*

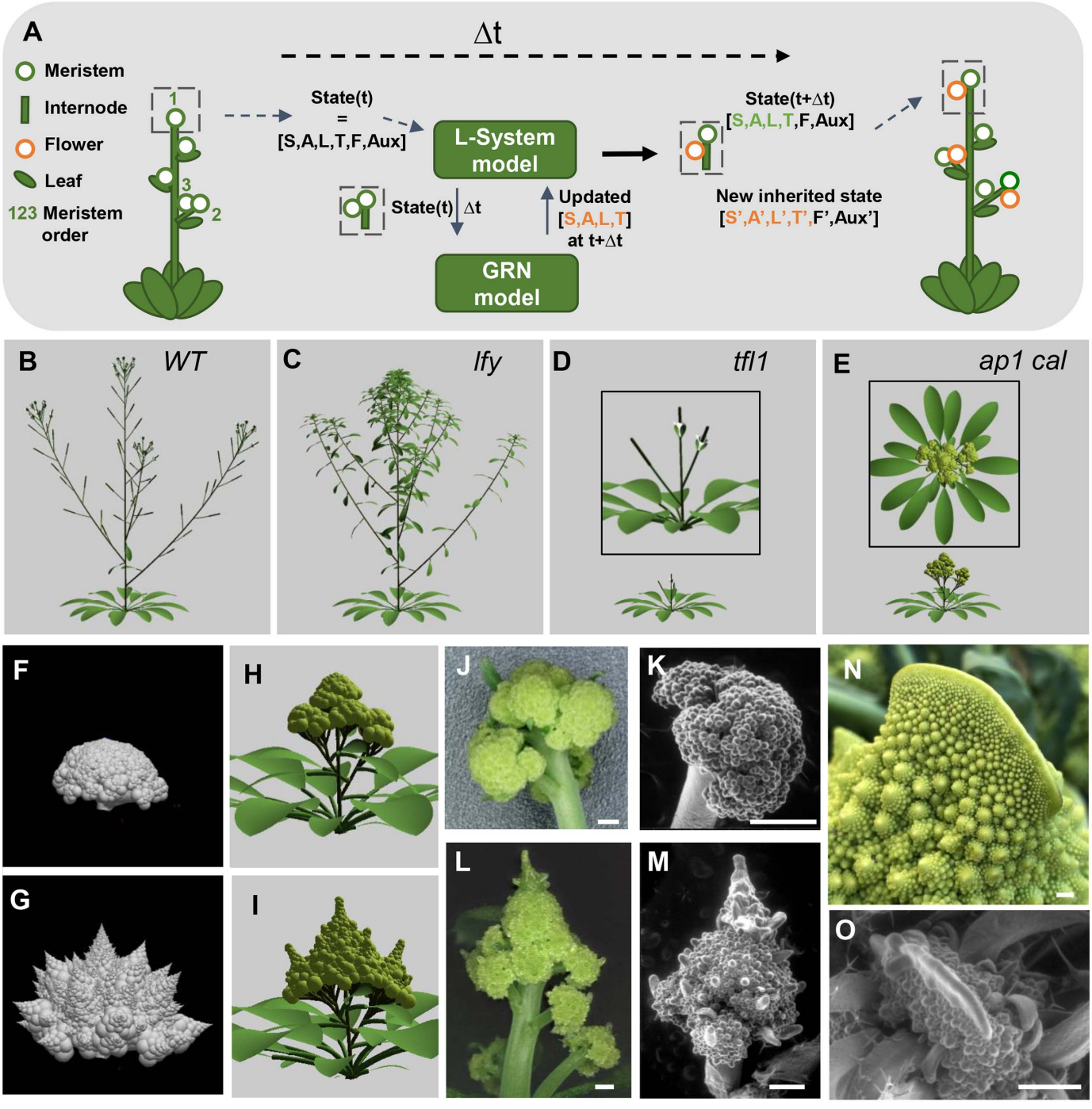

Fig. 4. Simulation and assessment of a GRN-based plant development model. (**A**) Schematic representation of the multiscale model of *Arabidopsis* development. Each meristem state is composed of signal levels (auxin, F) and a GRN steady state. At time *t*, the plant is made up of a collection of organs (left). At time *t*+Δ*t* (right), the model updates the signal levels and GRN state in each meristem. The steady state defines the identity of the meristems (vegetative, inflorescence, or flower) used to compute meristem lateral productions. Green numbers indicate meristem order. (**B** to **E**) Plant morphologies obtained in the WT (B), *lfy* (C), *tfl1* (D), and *ap1 cal* (E) simulations. (**F** to **I**) Simulated morphologies with constant [(F) and (H)] or increased [(G) and (I)] meristem production rate in a simplified model [(F) and (G)] and in the *Arabidopsis* model [(H) and (I)]. (**J** to **O**) Light micrographs [(J), (L), and (N)] and SEM [(K), (M), and (O)] of cauliflower structures in *Arabidopsis ap1 cal* [(J) and (K)], *Arabidopsis ap1 cal clv3* [(L), (M), and (O)], and Romanesco (N). The uninduced *AP1:GR* transgene is present in plants (J) to (M). Scale bars, 500 μm.

clv3 mutants (Fig. 4, N and O) (*37*); and (ii) the expression of *CLV3* (and possibly two other genes acting in the same pathway) (*38*) is lower in Romanesco curds than in cauliflowers (fig. S7). Altogether, these observations establish that meristem size regulates the final curd morphology through control of plastochron value.

These results reveal how fractal patterns can be generated through growth and developmental networks that alter identities and meristem dynamics. Our data, GRN, and growth models now clarify the molecular and morphological changes over time by which meristems gain different identities to form the highly diverse and fascinating array of plant architectures found throughout nature and crops.

REFERENCES AND NOTES

1. C. Godin, C. Golé, S. Douady, *Development* **147**, dev165878 (2020).
2. C. F. Quiros, M. W. Farnham, "The genetics of *Brassica oleracea*," in *Genetics and Genomics of the Brassicaceae*, R. Schmidt, I. Bancroft, Eds. (Springer, 2011), pp. 261–289.
3. D. V. Duclos, T. Björkman, *J. Exp. Bot.* **59**, 421–433 (2008).
4. L. B. Smith, G. J. King, *Mol. Breed.* **6**, 603–613 (2000).
5. N. Guo *et al.*, *BMC Biol.* **19**, 93 (2021).
6. J. L. Bowman, J. Alvarez, D. Weigel, E. M. Meyerowitz, D. R. Smyth, *Development* **119**, 721–743 (1993).
7. S. A. Kempin, B. Savidge, M. F. Yanofsky, *Science* **267**, 522–525 (1995).
8. G. Denay, H. Chahtane, G. Tichtinsky, F. Parcy, *Curr. Opin. Plant Biol.* **35**, 15–22 (2017).
9. A. Pajoro *et al.*, *J. Exp. Bot.* **65**, 4731–4745 (2014).
10. B. Thomson, F. Wellmer, *Curr. Top. Dev. Biol.* **131**, 185–210 (2019).
11. K. E. Jaeger, N. Pullen, S. Lamzin, R. J. Morris, P. A. Wigge, *Plant Cell* **25**, 820–833 (2013).
12. C. Espinosa-Soto, P. Padilla-Longoria, E. R. Alvarez-Buylla, *Plant Cell* **16**, 2923–2939 (2004).
13. F. Leal Valentim *et al.*, *PLOS ONE* **10**, e0116973 (2015).
14. P. Prusinkiewicz, Y. Erasmus, B. Lane, L. D. Harder, E. Coen, *Science* **316**, 1452–1456 (2007).
15. K. Goslin *et al.*, *Plant Physiol.* **174**, 1097–1109 (2017).
16. C. Ferrándiz, Q. Gu, R. Martienssen, M. F. Yanofsky, *Development* **127**, 725–734 (2000).
17. D. Bradley, O. Ratcliffe, C. Vincent, R. Carpenter, E. Coen, *Science* **275**, 80–83 (1997).
18. X. Hou *et al.*, *Nat. Commun.* **5**, 4601 (2014).
19. S. K. Yoo *et al.*, *Plant Physiol.* **139**, 770–778 (2005).
20. A. Serrano-Mislata *et al.*, *Development* **143**, 3315–3327 (2016).
21. R. V. Pérez-Ruiz *et al.*, *Mol. Plant* **8**, 796–813 (2015).
22. D. Reinhardt *et al.*, *Nature* **426**, 255–260 (2003).
23. P. A. Wigge, *Curr. Biol.* **21**, R374–R378 (2011).
24. J. Putterill, E. Varkonyi-Gasic, *Curr. Opin. Plant Biol.* **33**, 77–82 (2016).
25. C. Liu *et al.*, *Dev. Cell* **24**, 612–622 (2013).
26. O. J. Ratcliffe *et al.*, *Development* **125**, 1609–1615 (1998).
27. D. Weigel, J. Alvarez, D. R. Smyth, M. F. Yanofsky, E. M. Meyerowitz, *Cell* **69**, 843–859 (1992).
28. S. D. Michaels *et al.*, *Plant J.* **33**, 867–874 (2003).
29. Y. Zhu *et al.*, *Nat. Commun.* **11**, 5118 (2020).
30. L. Conti, D. Bradley, *Plant Cell* **19**, 767–778 (2007).
31. H. Chahtane *et al.*, *Plant J.* **74**, 678–689 (2013).
32. D. Weigel, O. Nilsson, *Nature* **377**, 495–500 (1995).
33. X. Sun *et al.*, *Environ. Exp. Bot.* **155**, 742–750 (2018).
34. M. Kieffer, M. P. Fuller, A. J. Jellings, *Planta* **206**, 34–43 (1998).
35. S. Douady, Y. Couder, *J. Theor. Biol.* **178**, 255–273 (1996).
36. Y. Refahi *et al.*, *eLife* **5**, e14093 (2016).
37. J. C. Fletcher, U. Brand, M. P. Running, R. Simon, E. M. Meyerowitz, *Science* **283**, 1911–1914 (1999).
38. M. Kitagawa, D. Jackson, *Annu. Rev. Plant Biol.* **70**, 269–291 (2019).
39. L. E. Watts, *Euphytica* **15**, 224–228 (1966).

ACKNOWLEDGMENTS

We thank A.-M. Chèvre, R. Immink, R. Simon, L. Ostergaard, and M. Benitez for advice; T. Vernoux, C. Zubieta, and H. Chahtane for proofreading and useful feedback on the manuscript; D. Tardy, E. Giraud, R. Dumas, and V. Martin (OBS, France) for providing cauliflower samples; L. Bousset Vaslin for images and branch counting; F. Boudon for help with L-Py; R. Immink (Wageningen, Netherlands), C. Ferrándiz (IBMCP; Spain), G. Coupland (MPIPZ, Germany), M. Ángel Blázquez (IBMCP, Spain), R. Amasino (UWM, USA), and the European *Arabidopsis* Stock Centre for providing seeds; V. Berger (CEA/DRF) for financing the Keyence microscope; and C. Lancelon-Pin (Plateau de microscopie électronique - ICMG. CERMAV-CNRS) for help with SEM experiments. **Funding:** This work was supported by the INRAE Caulimodel project (to F.P. and C.Go.); Inria Project Lab Morphogenetics (to C.Go., E.A., and F.P.); the ANR BBSRC Flower model project (to F.P. and C.Go.); the GRAL LabEX (ANR-10-LABX-49-01) within the framework of the CBH-EUR-GS (ANR-17-EURE-0003) (to F.P., G.T., M.L.M., and J.L.); the EU H2020 773875 ROMI project (to C.Go.); and the Spanish Ministerio de Ciencia Innovación and FEDER (grant no. PGC2018-099232-B-I00 to F.M.). **Author contributions:** C.Go. and F.P. conceived the study. C.Go., E.A., and E.F. performed the modeling. A.S.-M., C.Gi., D.B., F.M., F.P., G.T., M.M.K., M.L.M., and V.G. designed and performed the plant experiments. N.P. performed the confocal imaging experiment. J.L. analyzed the RNA-seq and genomic data. C.Go., F.P., and E.A. wrote the paper with contributions from all authors. **Competing interests:** The authors declare no competing interests. **Data and materials availability:** All data are available in the main paper or the supplementary materials. All plant materials are available upon request. Raw and processed RNA-seq data are available at GEO under accession no. GSE150627. All source codes to run the simulations are available as a supplementary archive file (descriptions of installation and execution are available as README.txt).

SUPPLEMENTARY MATERIALS

science.sciencemag.org/content/373/6551/192/suppl/DC1
Materials and Methods
Figs. S1 to S6
Tables S1 to S3
Movies S1 to S5
References (*40*–*108*)
Code Archive File: Architecture-Model.zip
MDAR Reproducibility Checklist

View/request a protocol for this paper from *Bio-protocol*.

15 January 2021; accepted 3 June 2021
10.1126/science.abg5999